CHEMISTRY OF MATERIALS
Cite This: Chem. Mater. 2018, 30, 5941−5950
Article
pubs.acs.org/cm

Synergistic Coupling of Metallic Cobalt Nitride Nanofibers and IrO_x Nanoparticle Catalysts for Stable Oxygen Evolution

Su-Ho Cho,[†,§] Ki Ro Yoon,[†,§] Kihyun Shin,[‡] Ji-Won Jung,[†] Chanhoon Kim,[†] Jun Young Cheong,[†] Doo-Young Youn,[†] Seok Won Song,[†] Graeme Henkelman,[‡] and Il-Doo Kim*[,†]

[†]Department of Materials Science and Engineering, Korea Advanced Institute of Science and Technology, 291 Daehak-ro, Yuseong-gu, Daejeon, 34141, Republic of Korea

[‡]Department of Chemistry and the Institute for Computational Engineering and Science, University of Texas at Austin, Austin, Texas 78712, United States

Supporting Information

ABSTRACT: The utilization of sustainable water electrolysis for hydrogen production is currently limited by sluggish kinetics of the oxygen evolution reaction (OER). The development of stable, highly active, and cost-effective OER catalyst supports would facilitate commercialization of water electrolysis technologies. In this study, we report for the first time the use of metallic cobalt nitride (Co_4N) nanofibers (NFs) as highly stable and conductive scaffolds for supporting Ir nanoparticles (NPs). The Ir catalysts supported on Co_4N NFs exhibit high OER activity and stability in alkaline media as compared with Ir catalysts supported on other materials (Co_3O_4 or carbon NFs) and commercial Ir/C. These results are attributed to the (i) efficient charge or mass transport between Ir NPs and metallic one-dimensional (1D) Co_4N NFs or interfibers, (ii) maintenance of the active oxidation state (Ir^{3+}) of Ir NPs induced by synergistic charge compensation between catalyst and support during OER, and (iii) long-term stability induced by strong metal−support interactions.

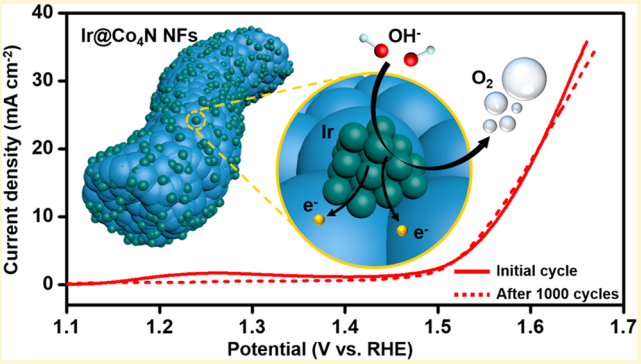

1. INTRODUCTION

The concern about ever-growing energy costs and global warming associated with fossil fuel use has prompted the development of sustainable approaches for energy production. Among the possible alternatives, hydrogen energy has recently gained attention and is gradually replacing fossil fuels in some applications such as fuel cell vehicles because it has been considered as an abundant, clean, and renewable resource with no harmful emission.[1] Water electrolysis is a promising way to generate hydrogen gas from water, but the sluggish reaction kinetics of the oxygen evolution reaction (OER) and the corresponding large overpotential at the anode limit the efficiency of water electrolyzers.[2] As a consequence, tremendous effort has been devoted to find better materials to efficiently catalyze OER for water electrolysis.[3,4]

Typically, noble metal based catalysts including Ir, Ru, and their oxides (IrO_2 and RuO_2) have been widely utilized as anode materials due to their outstanding OER activities and reasonable stabilities.[5−8] However, the high cost and scarcity of such noble metals limit their widespread industrial application. To address these issues, the expensive metals can be partially substituted by cheaper materials (e.g., Cu-doped IrO_x,[9] $IrCu_x$,[10,11] $IrNi_x$,[12,13] $IrNiO_x$,[14,15] etc.) to reduce the cost of the catalyst as well as enhance the catalytic activity. Additionally, precious metal catalysts can be combined with robust support materials to provide homogeneous distribution of catalysts.

Carbon materials are most widely utilized as support materials due to their high surface area, high electrical conductivity, and their tunable pore structure.[16,17] However, carbon materials are very corrosive at high potential (>1.5 V vs RHE), resulting in oxidation and irreversible loss of surface area.[18] Metal oxides are the second most prevalent support material, since they usually have exceptional durability toward corrosion or dissolution, stabilization of catalyst particles against agglomeration, and increased catalytic activity, which can be attributed to the strong interaction between metals (catalysts) and metal oxides (supports).[19] To date, Ir or IrO_2 nanoparticles (NPs) have been combined with robust oxide supports including TiO_2,[20,21] Nb-doped TiO_2,[22] Sb-doped SnO_2,[15,19,23] and ZnO.[24] Although enhanced electrochemical stability and performance have been achieved, key requirements such as sufficient electrical conductivity, available surface area, and structural stability under long-term operation should be further enhanced to make these support materials technically and economically viable.

Received: May 16, 2018
Revised: August 8, 2018
Published: August 9, 2018

DOI: 10.1021/acs.chemmater.8b02061
Chem. Mater. 2018, 30, 5941−5950

Scheme 1. Schematic Illustration for the Preparation of Ir@Co_4N NFs

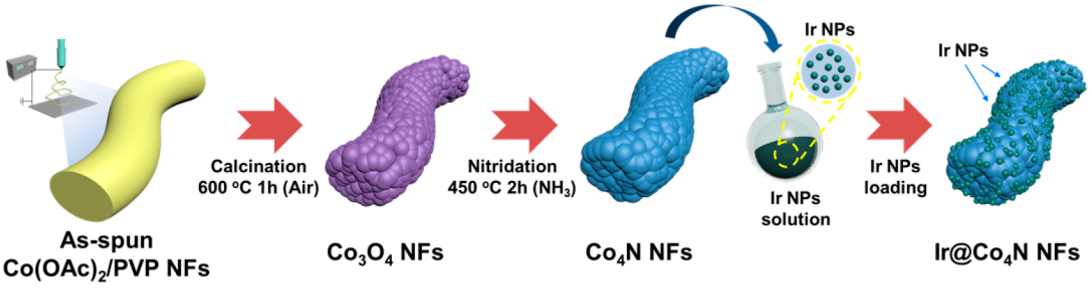

Metal carbides[25−27] or metal nitrides[28−30] have recently attracted much attention as supports or catalytic materials by themselves in electrocatalysis due to their superior chemical and physical robustness and high metallic conductivity. Among them, cobalt nitride (Co_4N) exhibits superior OER activity and stability in alkaline medium among other cobalt-based compounds.[31,32] The outstanding performance of Co_4N is attributed to the metallic electrical conductivity of Co_4N cores and stable surface active sites that can facilitate oxidation of OH^- into O_2. Nonetheless, the possibility of Co_4N as a support material has rarely been investigated in water electrolysis.

In this regard, we have devised a novel composite material involving Co_4N nanofibers (NFs) as support materials and small Ir NPs as the primary OER catalytic components. The combination of one-dimensional (1D) fibers scaffold and 0D catalysts is known to be an ideal configuration in electrocatalysis because of (i) high exposure and dispersion of the catalytic particles on the surface of the supporting material, (ii) directional and fast charge transfer along the 1D fiber channels, and (iii) efficient mass (electrolyte) diffusion between interfiber spaces.[33,34] Scheme 1 illustrates the method used to synthesize the Co_4N NFs supported Ir NPs (Ir@Co_4N NFs) catalysts. Co_4N NFs were obtained from conventional electrospinning followed by a two-step heat treatment: calcination and nitridation.[31,35] The Ir NPs of 2.6 nm in diameter were prepared via a conventional polyol method.[36] The premade Co_4N NFs were soaked in Ir NPs dispersed solution and stirred vigorously. Finally, the Co_4N NFs and Ir NPs dispersed solution was evaporated at 50 °C for 12 h, followed by annealing at 300 °C for 1 h in an Ar atmosphere.

The Ir@Co_4N NFs exhibited excellent electrocatalytic activity for OER in alkaline media and superior electrochemical stability compared to Ir catalysts supported on Co_3O_4 NFs and carbon nanofibers (CNFs) (Ir@Co_3O_4 and Ir@CNFs) and commercial Ir/C catalysts. We have demonstrated that the outstanding performance of Ir@Co_4N NFs in OER could be attributed to (i) the unique 1D metallic Co_4N NFs for efficient charge transport, (ii) synergistic charge compensation for maintaining the catalytic active phase of Ir NPs, and (iii) improved durability of Ir NPs on robust supports induced by a strong metal−support interaction.

2. EXPERIMENTAL SECTION

2.1. Materials. Cobalt(II) acetate tetrahydrate ($Co(OAc)_2{\cdot}4H_2O$, Sigma-Aldrich), poly(vinylpyrrolidone) (PVP, M_w ∼ 1 300 000, Sigma-Aldrich), and *N*,*N*-dimethylformamide (DMF, 99.8%, Sigma-Aldrich) were prepared for the synthesis of Co_3O_4 and Co_4N NFs. Hexachloroiridic acid hydrate ($H_2Cl_6Ir{\cdot}xH_2O$, 99.98%, Sigma-Aldrich), ethylene glycol (EG, 99.5%, SAMCHUN Chemical), and PVP (M_w ∼ 10 000, Sigma-Aldrich) were prepared for the synthesis of monodispersed Ir NPs. Nafion solution (Nafion 117 solution, ∼5% in a mixture of lower aliphatic alcohols and water) and isopropyl alcohol (IPA) were purchased from Sigma-Aldrich.

2.2. Preparation of Co_3O_4 NFs and Co_4N NFs. The Co_3O_4 NFs were synthesized via a simple electrospinning method and a subsequent calcination step. Amounts of 3 g of $Co(OAc)_2{\cdot}4H_2O$ and 1 g of PVP (M_w ∼ 1 300 000) were dissolved in 8 g of DMF at 50 °C with magnetic stirring at 500 rpm for 12 h. The homogeneously mixed viscous solution was transferred into a plastic syringe with a stainless steel needle (25 gauge) that was equipped on the electrospinning machine (Nano NC, Korea). A stainless steel foil was used as a grounded current collector that was placed at a distance of 15 cm from the needle tip. A high dc voltage (15 kV) was applied on the tip of needle, and the electrospinning solution was subsequently pulled out with the flow rate of 30 μL min^{-1}. Then, elongated as-spun fibers were collected on the stainless steel foil. The as-spun $Co(OAc)_2$/PVP composite NFs were calcined at 600 °C for 1 h with a ramping rate of 5 °C min^{-1} in an air atmosphere. After calcination, black Co_3O_4 NFs were obtained.

For the synthesis of Co_4N NFs, the Co_3O_4 NFs were placed in an Ar-filled tube furnace and nitridized at 450 °C for 2 h (7.5 °C min^{-1}) with a continuous NH_3 gas flow (100 sccm). After cooling down the furnace to room temperature, the Co_4N NFs were obtained.

2.3. Preparation of Ir NPs Solution. The monodisperse Ir NPs were synthesized by using a polyol method.[36] An amount of 45 mL of EG was heated to 120 °C in an oil bath, and 5 mL of $H_2IrCl_6{\cdot}xH_2O$ dissolved EG (100 mg mL^{-1}) was added into the hot EG solution. Subsequently, 20 mL of PVP (M_w ∼ 10 000) dissolved EG (10 mg mL^{-1}) was added with an injection rate of 2 mL min^{-1} and the solution was kept at 150 °C for 1 h. After cooling down, acetone was added to the Ir solution (acetone/Ir solution = 4:1 v/v), and the solution was centrifuged at 3000 rpm for 10 min. The segregated supernatant was discarded and replaced with ethanol. The Ir colloidal solution was then diluted to 0.894 mg mL^{-1} in ethanol for use.

2.4. Preparation of Ir@Co_4N NFs. For the synthesis of the Co_4N NFs-supported Ir NPs (Ir@Co_4N NFs), certain amounts of Co_4N NFs were added to the Ir colloidal solution and dispersed using sonication for 1 h. The resulting suspension was stirred for 30 min and kept in a convection oven at 50 °C for 12 h to evaporate the solvent. The dried mixture of Ir NPs and Co_4N NFs was thermally treated at 300 °C for 1 h in Ar atmosphere. For purposes of comparison, CNFs- and Co_3O_4 NFs-supported Ir NPs (Ir@CNFs and Ir@Co_3O_4 NFs) were prepared using the same procedure described above.

2.5. Materials Characterization. The morphologies and structures of the catalysts were examined by scanning electron microscopy (SEM, XL-30 SFEG, Philips, U.S.A.) and field emission transmission electron microscopy (FE-TEM, Tecnai G2 F30 S-Twin, FEI, Netherlands) with energy-dispersive X-ray spectrometry (EDS) analysis. The X-ray diffraction (XRD) patterns of Co_3O_4 NFs, Co_4N NFs, and Ir@Co_4N NFs were measured by an X-ray diffractometer (D/MAX-2500, Rigaku, Japan) using Cu Kα (λ = 1.54 Å) radiation. The amounts of Ir NPs in the catalysts were analyzed by a inductively coupled plasma mass spectrometer (ICP-MS, Agilent ICP-MS 7700S, Agilent, U.S.A.). The surface analysis of catalysts was performed by X-

DOI: 10.1021/acs.chemmater.8b02061
Chem. Mater. 2018, 30, 5941−5950

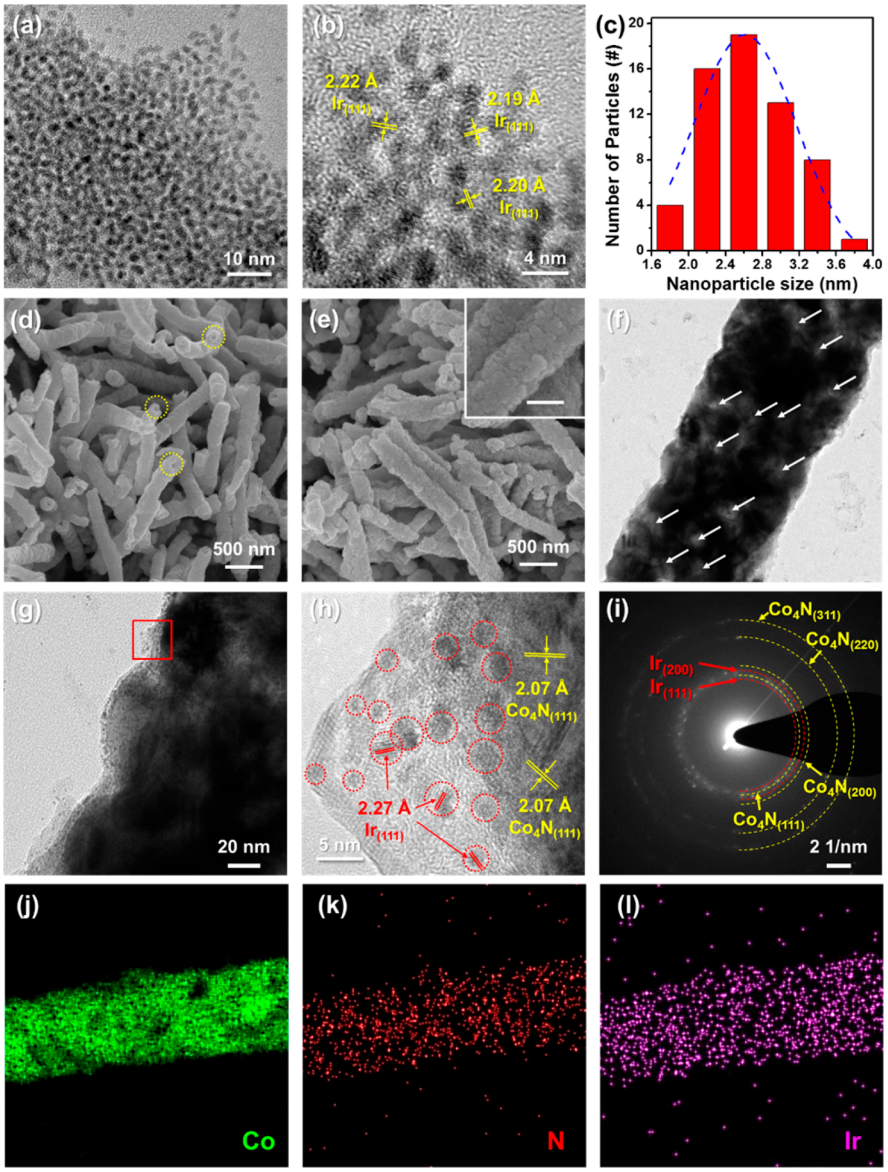

Figure 1. TEM images of Ir NPs with (a) low and (b) high magnifications. (c) Particle size distribution of Ir NPs. SEM images of (d) Co_4N NFs and (e) Ir@Co_4N NFs (scale bar in inset is 200 nm). TEM images of Ir@Co_4N NFs with (f) low (g) medium, and (h) high magnifications. (i) SAED patterns of Ir@Co_4N NFs. EDS elemental maps of Ir@Co_4N NFs: (j) Co, (k) N, and (l) Ir atoms.

ray photoelectron spectroscopy (XPS) measurement (Thermo VG Scientific, Germany) with Kα radiation as excitation source.

2.6. Electrochemical Tests of Ir@Co_4N NFs. Electrochemical measurements were performed in a three-electrode system on single-channel potentiostat (ZIVE SP1, Wonatech, Korea). In a typical procedure, the catalyst ink suspension contained 50 μL of Nafion solution (5%) and 5 mg of catalyst dispersed in 1.25 mL of solvent composed of DI water and IPA with 3:1 v/v. The ink suspension was sonicated for 30 min, and then dropped on a glassy carbon electrode (GCE) with a catalyst loading mass of 0.285 mg cm^{-2}. The catalyst-loaded GCE was equipped on the potentiostat as the working electrode. Pt coil and Hg/HgO (filled with 1 M NaOH, $E^0_{Hg/HgO}$ = 0.140 V vs RHE) were used as the counter and reference electrode, respectively. All electrochemical measurements were performed in an O_2-saturated 0.1 M KOH solution (pH = ~13). The measured potentials reported in our work were converted to the reversible hydrogen electrode (RHE) through the Nernst equation, $E_{RHE} = E_{Hg/HgO} + 0.140\ V + 0.059pH$, and have been corrected by *IR* compensation. Linear sweep voltammetry (LSV) was conducted in the potential range of 0.0−1.0 V (vs Hg/HgO) with a scan rate of 5 mV s^{-1}. Electrochemical impedance spectroscopy (EIS) tests were performed by applying an ac voltage with a 10 mV amplitude in a frequency range from 1 MHz to 0.1 Hz. To investigate the stability of the catalysts, cyclic voltammetry (CV) scanning was carried out for 1000 cycles in a potential range from 0.0 to 0.8 V (vs Hg/HgO) with a scan rate of 100 mV s^{-1}, and chronoamperometric experiments were performed at 1.6 V (vs RHE) for 24 h.

2.7. Density Functional Theory Calculations. The adsorption energies of Ir NPs on the Co_4N and turbostratic doped carbon were calculated to evaluate the durability of the supported catalysts. Ir NPs consisting of 4, 5, 9, 10, and 21 Ir atoms were considered, to determine trends in the adsorption energy as a function of particle size. A Co_4N (111) surface was constructed with a 3 × 3 supercell containing six atomic layers with the bottom two layers fixed in their bulk positions. We considered turbostratic doped carbon to describe CNF; detailed information about the turbostratic doped carbon model has been described in our previous study.[37] Both systems contained a 10 Å vacuum gap to isolate the slabs from their periodic images.

GGA-level spin-polarized density functional theory (DFT) calculations were performed with the Vienna ab initio simulation package (VASP).[38] The Perdew−Burke−Ernzerhof (PBE) functional

DOI: 10.1021/acs.chemmater.8b02061
Chem. Mater. 2018, 30, 5941−5950

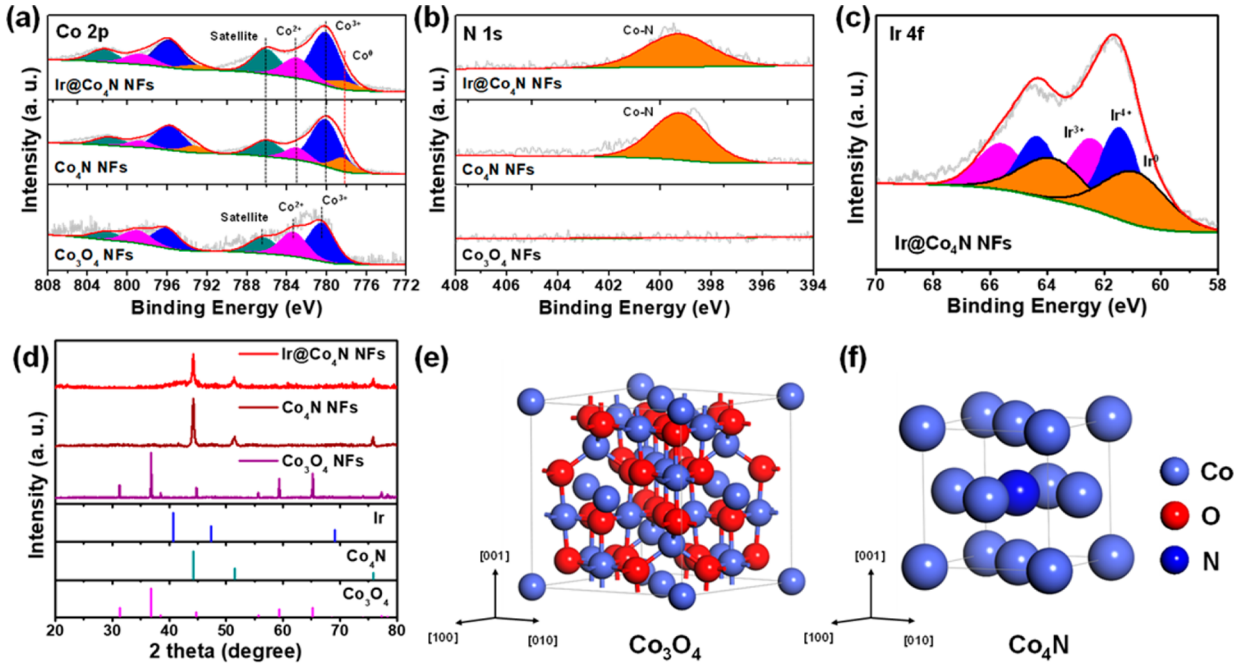

Figure 2. XPS spectra in (a) Co 2p, (b) N 1s, and (c) Ir 4f regions for Co_3O_4 NFs, Co_4N NFs, and Ir@Co_4N NFs. (d) XRD results of Co_3O_4 NFs, Co_4N NFs, and Ir@Co_4N NFs. Crystallographic data of (e) Co_3O_4 and (f) Co_4N.

was employed to describe electronic exchange and correlation.[39] The interaction between the ionic cores and the valence electrons were treated within the projector augmented wave framework.[40] In this study, the cutoff energy was set to 400 eV and the Brillouin zone was sampled at 2 × 2 × 1 with the Monkhorst–Pack scheme. The convergence criteria for the electronic structure and geometry were set to 10^{-5} eV and 0.01 eV $Å^{-1}$, respectively. Adsorption energies of Ir NPs were calculated as

$$E_{ads} = E_{IrNP+Support} - (E_{Support} + E_{IrNP})$$

Here, E_{ads} is the adsorption energy of a supported Ir NP, $E_{IrNP + Support}$ is the total energy after binding of the Ir NP on the support, $E_{Support}$ is the total energy of isolated clean support, and E_{IrNP} is the total energy of an isolated Ir NP.

3. RESULTS AND DISCUSSION

The microstructures of the synthesized Ir NPs, Co_4N NFs, and Ir@Co_4N NFs were characterized by SEM and TEM measurements (Figure 1). As shown in Figure 1a, the Ir colloidal solution prepared by the polyol method contained uniform and monodispersed Ir NPs due to the capping effect of PVP.[36] The observed interplane distances in the NPs are between 2.19 and 2.22 Å, corresponding to the (111) facet of metallic Ir (Figure 1b).[19] The average size of the Ir NPs was 2.6 nm (Figure 1c).

Figure S1 shows that Co_3O_4 NFs have a clear 1D structure with an average diameter of 270 nm. The surface of the nanofibers consists of densely ordered Co_3O_4 grains (Figure S1b). The high-resolution TEM (HRTEM) image and the selected-area electron diffraction (SAED) pattern indicate that the Co_3O_4 NFs have a polycrystalline spinel-type structure with (111) plane oriented surfaces (Figure S1, parts c and d). By subsequent annealing at 450 °C in the presence of NH_3 gas, the Co_3O_4 NFs were converted into Co_4N NFs. As shown in Figure 1d, the overall 1D structure was maintained through the nitridation process. The grooves at the edge of the NFs (yellow dashed circles), which appeared in both the Co_3O_4 and Co_4N NFs, were induced by Kirkendall's effect during electrospinning and thermal treatments.[41] Interestingly, the grain size of Co_4N became smaller, to sub-10 nm, and numerous mesopores were formed around the NFs (Figure S2a). Scanning TEM (STEM) more clearly shows the existence of mesopores as dark fields in the NFs (Figure S2b). These microstructural changes are attributed to the difference of crystalline structure between Co_3O_4 and Co_4N and the partial gasification of the oxide supports caused by NH_3 etching.[42,43] The HRTEM image of Co_4N NFs shows distinct lattice fringes of 2.07 Å, which are consistent with the (111) plane of Co_4N.[37]

After Ir NPs loading, the surface of the Co_4N NFs became rougher, but the overall morphology of the NFs was well-maintained (Figure 1e). We could confirm the existence of mesopores in the Co_4N NFs through TEM observation as indicated by white arrows (Figure 1f). As shown in the extended TEM image (Figure 1g), the spherical Ir NPs are observed on the surface of the Co_4N NFs. From the HRTEM image (Figure 1h), we confirm that the Ir NPs were crystalline, exhibiting (111) planes of metallic Ir (red dashed circles). As a catalyst support material, Co_4N NFs were also preserved after loading of Ir NPs with a well-defined lattice spacing of 2.07 Å, corresponding to the (111) plane of Co_4N. The clear ring patterns in the SAED result (Figure 1i) also support the coexistence of both Ir and Co_4N species as polycrystalline structures. Energy-dispersive X-ray spectroscopy analysis (Figure 1j–l) reveals the complete formation of nitride compounds (Co_4N) and a uniform distribution of Ir species on the Co_4N NFs. These comprehensive results indicate that ~2.6 nm sized Ir NPs were supported on the surface of mesoporous Co_4N NFs without significant aggregation.

For the purpose of comparison, we also prepared Ir NPs supported on CNFs (Ir@CNFs). The CNFs, that were prepared by electrospinning and a subsequent carbonization annealing, exhibited a 1D structure with a smooth surface and an uniform diameter of 630 nm (Figure S3a). The Raman spectrum of CNFs (Figure S3b) shows two major peaks at

DOI: 10.1021/acs.chemmater.8b02061
Chem. Mater. 2018, 30, 5941–5950

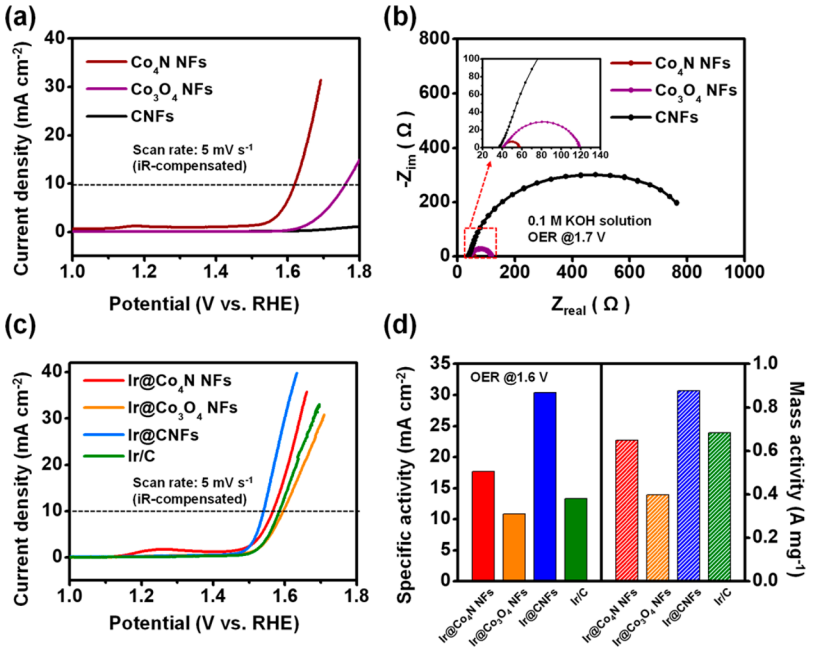

Figure 3. (a) Electrocatalytic OER performance and (b) electrochemical impedance spectroscopy (EIS) curves of CNFs, Co_3O_4 NFs, and Co_4N NFs. (c) Electrocatalytic OER performance and (d) specific and mass activities (based on the Ir contents) of Ir@Co_4N NFs, Ir@Co_3O_4 NFs, Ir@CNFs, and commercial Ir/C catalysts. All measurements were performed in an Ar-purged 0.1 M KOH solution.

approximately 1348 and 1590 cm^{-1}, assigned to the D and G bands. The relative intensity of the D and G band peaks (I_D/I_G) is used to estimate the amount of disorder in the carbon structure, and the I_D/I_G value of 0.963 is similar to the turbostratic carbon structure predominant in electrospun CNFs as reported in the literature.[37] In order to prepare Ir@CNFs, Ir NPs were attached on the CNFs in the same manner with Ir@Co_4Ns, and their microstructures are displayed in Figure S4.

The chemical and structural properties of Co_3O_4 NFs, Co_4N NFs, and Ir@Co_4N NFs were investigated with XRD and XPS. As shown in Figure 2a, the Co 2p spectra of Co_3O_4 NFs can be deconvoluted into Co^{3+}, Co^{2+}, and satellite peaks at 780.53, 783.43, and 786.53 eV, respectively.[37] The coexistence of Co^{3+} and Co^{2+} is attributed to the spinel-type Co_3O_4 as illustrated in Figure 2e. After the nitridation process, the binding energy of metallic Co^0 bond centered at 778.58 eV was detected in Co_4N NFs. The existence of mixed valence of cobalt ions (Co^{3+} and Co^{2+}) in Co_4N NFs implies that the surface of Co_4N NFs includes slightly oxidized species (CoO_x) as reported in previous studies.[31] Their binding energies were maintained when the Ir NPs were introduced at the surface. In the N 1s region (Figure 2b), no specific bonds were detected in Co_3O_4 NFs, while clear Co−N bond appeared in Co_4N NFs and Ir@Co_4N NFs. These results indicate that the surface chemical composition was changed and that N species were definitely introduced in the nitridation step. From the XRD patterns, we could observe clear crystalline changes from Co_3O_4 to Co_4N after the nitridation process (Figure 2d). The XRD pattern of Co_3O_4 NFs was well-matched with previously reported spinel-type Co_3O_4 (JCPDF no. 42-1467).[35] For Co_4N NFs, the XRD patterns were matched with Co_4N phases through (111), (200), and (220) planes at 44.2°, 51.5°, and 75.9°, respectively, as reported in the literature.[37] The Co_4N is known to have a face-centered crystal (fcc) structure in which four Co atoms are close-packed and a N atom is placed at the center of the unit cell as illustrated in Figure 2f. The crystalline structure of Co_4N was not significantly changed after Ir loading, evidenced by our XPS and XRD results. The Co_4N NFs exhibit a positive temperature-dependent resistance behavior, consistent with metallic conduction (Figure S5). The metallic property of Co_4N NFs results in electron delocalization and brings efficient charge transfer between the surface of the catalysts and the current collector, which is a critical requirement of an effective support material for electrocatalysis. For Ir@Co_4N NFs, the spectrum of Ir 4f was dominated by Ir^{4+} bonds (1.59 atom %) and followed by Ir^0 (0.7 atom %) and Ir^{3+} (0.44 atom %) bonds, implying the evolution of oxidized iridium (IrO_x) covering the metallic Ir core in NPs.[44] Considering the probe depth of the X-ray in the XPS analysis, the thickness of this oxide layer should be less than 2 nm.

To assess the electrochemical properties of the pristine support materials, we first carried out OER tests by comparing Co_3O_4 NFs, Co_4N NFs, and CNFs without Ir catalysts. Figure 3a compares the current−potential response of Co_3O_4 NFs, Co_4N NFs, and CNFs in an O_2-purged 0.1 M KOH solution. Co_4N NFs and Co_3O_4 NFs show OER overpotentials (η) of 0.44 and 0.53 V at 10 mA cm^{-2}, respectively, while a negligible response was observed for the pristine CNFs. The OER performance of Co-based catalysts can be explained by the presence of Co^{3+}/Co^{2+} redox surface sites, and the OER activity of the pristine Co_4N NFs is comparable to what has recently been reported for a Co_4N catalyst.[31] Figure 3b depicts the Nyquist plots of EIS for Co_4N NFs, Co_3O_4 NFs, and CNFs. A reduction of the semicircle radii, related to the charge-transfer process during the OER, supports the higher catalytic activity of Co_4N NFs as compared to Co_3O_4 NFs.

The initial OER activities of Ir NPs loaded on various support materials including Ir@Co_4N NFs, Ir@Co_3O_4 NFs, and Ir@CNFs were measured by LSV and compared with commercial Ir/C (20 wt %, Fuel Cell Store) as shown in

DOI: 10.1021/acs.chemmater.8b02061
Chem. Mater. 2018, 30, 5941−5950

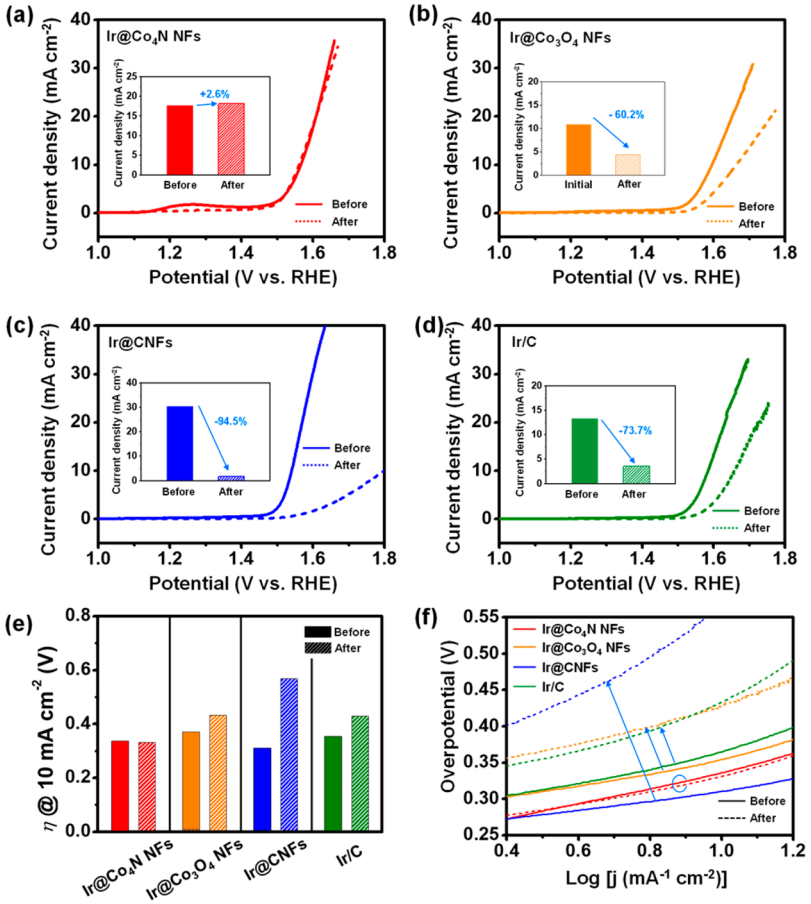

Figure 4. Linear sweep voltammetry (LSV) curves before and after a stability test: (a) Ir@Co_4N NFs, (b) Ir@Co_3O_4 NFs, (c) Ir@CNFs, and (d) commercial Ir/C catalysts with a scan rate of 5 mV s^{-1}. Inset: bar chart of corresponding current densities at 1.6 V. (e) Comparison of overpotentials to reach 10 mA cm^{-2} before and after cycling. (f) Tafel plots of Ir@Co_4N NFs, Ir@Co_3O_4 NFs, Ir@CNFs, and commercial Ir/C catalysts before and after the stability test.

Figure 3c. The slight shoulder appeared at around 1.2 V in Ir@Co_4N NFs was attributed to the electrochemical oxidation of Co_4N under the positive bias, which was similarly observed in the polarization curves of pristine Co_4N NFs (Figure 3a). The shoulder was not observed after further cycling test (Figure 4a), which means that the surficial layer of Co_4N was slightly oxidized to catalytically active CoO_x without excessive oxidation of the core Co_4N phase, as previously reported.[31] Interestingly, the Ir@CNFs system shows the best OER activity followed by Ir@Co_4N NFs, Ir/C, and Ir@Co_3O_4 NFs with overpotential values to drive 10 mA cm^{-2} of 0.310, 0.336, 0.354, and 0.365 V, respectively. The superior performance of Ir@CNFs can be explained by the highest electrical conductivity of CNFs (~20 Ω sq^{-1}) among the samples.[37] The specific activity of Ir@Co_4N NFs, Ir@Co_3O_4 NF, Ir@CNFs, and Ir/C obtained at a potential of 1.6 V were 17.68, 10.87, 30.40, and 13.34 mA cm^{-2}, respectively (Figure 3d, left column). When we considered the Ir mass activity in the catalysts, calculated from the inductively coupled plasma optical emission spectrometry (ICP-OES, Table S1), Ir@CNFs still exhibited the highest activity of 0.87 A mg_{Ir}^{-1} followed by Ir/C (0.68 A mg_{Ir}^{-1}), Ir@Co_4N NFs (0.65 A mg_{Ir}^{-1}), and finally Ir@Co_3O_4 NFs (0.39 A mg_{Ir}^{-1}). These results indicate that the initial OER activity at high potential is largely affected by the electrical conductivities of the support materials. Nevertheless, the mass activity of Ir@Co_4N NFs exhibits a high value among the reported values of Ir-based catalysts supported by various materials in previous literatures (Table S4).

To check the stability of the prepared samples (Ir@Co_4N, Ir@Co_3O_4 NFs, and Ir@CNFs), we conducted LSV tests after 1000 cyclic potential sweeps between 0.9 and 1.7 V. For Ir@Co_4N NFs, the OER curve exhibited a similar shape with 2.8% increased current density at 1.6 V after cycling test (Figure 4a). On the other hand, Ir@Co_3O_4 NFs shows a drastic performance decline by 60.2% after 1000 cycles (Figure 4b). Compared to the stable performance of pristine Co_3O_4 NFs after 1000 cycles (Figure S6), there is a significant reduction of OER performance of Ir@Co_3O_4 NFs. The Ir catalysts supported on carbon-based materials (Ir@CNFs and Ir/C) exhibit drastic degradation after the cycling test. As can be seen in the inset of Figure 4c, almost 94.5% loss of initial current density was measured after the stability test. Similarly, the OER performance of the Ir/C catalyst showed a performance decline by 73.7% at 1.6 V after cycling (Figure 4d). The results show that there is a correlation between improved OER stability of catalysts and support materials.

As shown in Figure 4e, Ir@Co_4N NFs has similar η values before and after cycling, with only a slight change from 0.336 to 0.331 V, while the other samples exhibited significantly increased η values after the cycling test. In particular, the Tafel slope of the Ir@Co_4N NFs increased slightly from 94.5 to 102.92 mV dec^{-1} (Figure 4f). In contrast, drastic increases of the Tafel slopes for Ir@Co_3O_4 NFs (from 103.42 to 154.25

DOI: 10.1021/acs.chemmater.8b02061
Chem. Mater. 2018, 30, 5941−5950

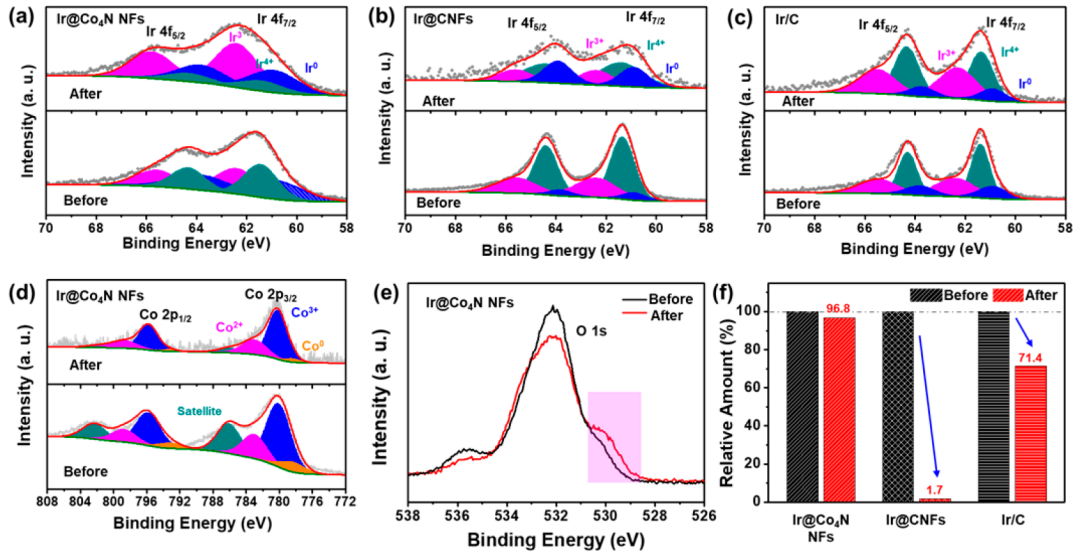

Figure 5. XPS Ir 4f spectra of (a) Ir@Co_4N NFs, (b) Ir@CNFs, and (c) commercial Ir/C catalysts before and after cycling tests (1000 cycles). (d) XPS Co 2p and (e) O 1s spectra of Ir@Co_4N NFs before and after cycling tests. (f) Relative quantities of Ir atoms in Ir@Co_4N NFs, Ir@CNFs, and commercial Ir/C catalysts before and after cycling tests.

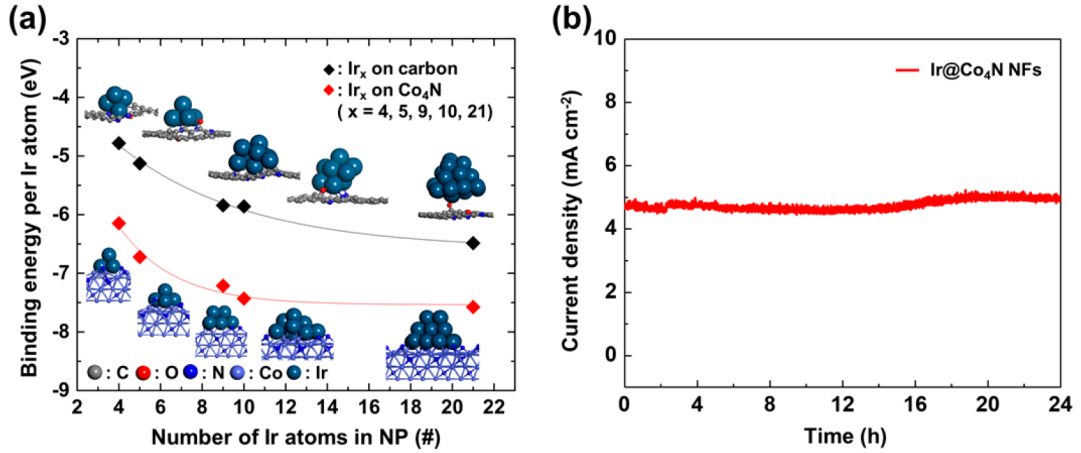

Figure 6. (a) Adsorption energy of Ir_x NPs on the Co_4N and turbostratic doped carbon. (b) Chronoamperometric response of Ir@Co_4N NFs at 1.6 V (vs RHE).

mV dec^{-1}), Ir@CNFs (from 70.53 to 240.02 mV dec^{-1}), and Ir/C (from 114.73 to 158.92 mV dec^{-1}) were observed.

Oxidation states of Ir NPs in Ir@Co_4N NFs, Ir@CNFs, Ir/C before and after potential cycling tests were investigated with XPS. As shown in Figure 5a–c, the Ir 4f spectrum for all samples can be deconvoluted into a contribution of Ir^0 (60.9 eV), Ir^{4+} (61.4 eV), and Ir^{3+} (62.4 eV) species along with their respective satellites.[10,45] It is noteworthy that the 4f spectrum of Ir@Co_4N NFs and Ir@CNFs exhibited different shapes, indicating that the electronic structure of the Ir NPs is changed on the different support materials. The relative quantities of Ir 4f spectra before and after cycling test are summarized in Table S2.

In their initial state, the majority of Ir 4f states correspond to Ir^{4+} for all samples. However, sharp Ir^{4+} peaks were detected in Ir@CNFs and Ir/C, implying that Ir NPs tend to be more oxidized on the carbonaceous surface. For Ir@Co_4N NFs, a significant amount of Ir^{3+} associated with oxygen vacancies increased, while other peaks (Ir^{4+} and Ir^0) decreased after the cycling test (Table S2). On the other hand, the Ir^{4+} peaks were maintained in Ir@CNFs and Ir/C after cycling (Figure 5, parts b and c).

To determine the origin of the lower oxidation state (Ir^{3+}) in Ir@Co_4N NFs, we monitored changes in the Co 2p spectra before and after potential cycling. As shown in Figure 5d (lower column), the Co 2p spectra appeared similar to Co^0, Co^{3+}, and Co^{2+} states at binding energies of 778.4, 780.1, and 783.0 eV in the initial Ir@Co_4N NFs sample. After potential cycling, the surface of Co_4N had more oxidized species including Co^{3+} and Co^{2+}, or more quantitatively, the "Co^0/(Co^{2+} + Co^{3+})" ratio decreased from 8.0% to 3.3% upon cycling (Figure S8). Furthermore, the O 1s XPS spectra (Figure 5e) show an increase in the binding energy ranging from 530 to 531.5 eV, alluding to the evolution of CoO_x species as well as $IrO_x(OH)_y$ on the surface, which are known to catalytically active for OER.[7,10,14,46,47] On the basis of the above observation, it is reasonable to assert that there is a direct correlation between the chemical changes of the Co_4N NFs surface and Ir NPs. As evidenced by XPS, the surface oxidation of Co_4N during OER plays a significant role in preserving the active Ir^{3+} state of Ir NPs.

DOI: 10.1021/acs.chemmater.8b02061
Chem. Mater. 2018, 30, 5941−5950

One of the critical factors causing performance degradation of the catalysts from their initial performance is detachment or dissolution of the catalytic material from their supports during OER.[19,48] Figure 5f compares the relative amount of Ir in the catalyst before and after cycling. The calculated Ir losses of Ir@Co_4N NFs, Ir@CNFs, and Ir/C were 3.2%, 98.3%, and 28.6% of their initial Ir composition, respectively. These results imply that Ir NPs were well-anchored to the Co_4N NF support even after vigorous OER cycling, while Ir NPs were easily detached from the CNFs and the commercial Vulcan carbon in the Ir/C catalyst during OER testing. Overall, these results provide evidence that the Ir component has better sustainability on the Co_4N NFs as catalyst support compared to other carbonaceous supports.

To better understand the strong metal−support interaction, we calculated the adsorption energy of Ir NPs on Co_4N supports.[49] As shown in Figure 6a, the E_{ads} of Ir NPs increases with the number of Ir atoms in the clusters. The E_{ads} of Ir_{21} NP (which has an estimated particle size of ∼0.8 nm) were −7.53 eV on the Co_4N surface and −6.36 eV at the defect site of turbostratic doped carbon. More negative E_{ads} values represent stronger binding of Ir NPs on the scaffold surface.[28−30] Although the particle sizes in our simulations are smaller than the synthesized Ir NPs in the experiment, there is a clear trend in Figure 6a showing that larger Ir NPs will have stronger binding energies on the Co_4N than that on the turbostratic doped carbon. The stability of the catalytic activity and the high durability of the catalyst can be attributed to a strong interaction between metal (Ir NPs) and support (Co_4N NFs), preventing aggregation or detachment of active particles. The various E_{ads} values for supported clusters with different number of Ir atoms (Ir_x, x = 4, 5, 9, 10, 21) are listed in Table S3.

Finally, we evaluated the long-term stability of Ir@Co_4N NFs by chronoamperometric response (Figure 6b), which was performed at 1.6 V (vs RHE). The Ir@Co_4N NFs exhibit excellent stability with no obvious decay for over 24 h. However, Ir@CNFs show fast degradation of their initial current density value (Figure S9). These results demonstrate that the Co_4N NFs act as a robust and promising support material for OER catalysts in terms of (i) high electrical conductivity due to the electron delocalization of Co_4N, (ii) stability of their active phase by synergistic charge compensation, and (iii) formation of strong adhesion between metal NPs and nitride NFs.

4. CONCLUSION

In this work, we first reported metallic Co_4N NFs as a stable and robust support material for efficient OER in water electrolysis. The Co_4N NFs were prepared via a facile electrospinning technique, and Ir NPs prepared by a polyol method were loaded onto the surface of Co_4N NFs. The prepared Ir@Co_4N NFs exhibit high OER activity and excellent stability (over 1000 cycles) in alkaline media as compared with commercial Ir/C. We demonstrated that Ir NPs maintain surface-active Ir^{3+} when they are loaded on Co_4N NFs, which undergo surficial oxidation during OER. Furthermore, a strong metal−support interaction between Ir NPs and Co_4N NFs suppresses the dissolution or detachment of the Ir NPs from the Co_4N NF support, enabling long-term electrochemical stability. This work provides a new avenue for the development of a new class of supports which have high electrical conductivity, high compatibility with catalysts, and enhanced stability.

■ ASSOCIATED CONTENT

Supporting Information

The Supporting Information is available free of charge on the ACS Publications website at DOI: 10.1021/acs.chemmater.8b02061.

Graphical and tabular characterization information including a table of ICP-OES analysis, SEM images, TEM images, XRD, and additional graphical information on electrochemical measurement (PDF)

■ AUTHOR INFORMATION

Corresponding Author

*E-mail: idkim@kaist.ac.kr.

ORCID

Graeme Henkelman: 0000-0002-0336-7153

Il-Doo Kim: 0000-0002-9970-2218

Author Contributions

§S.-H.C. and K.R.Y. contributed equally to this work.

Notes

The authors declare no competing financial interest.

■ ACKNOWLEDGMENTS

This work was supported by the Korea CCS R&D Center (KCRC) grant funded by the Korea government (Ministry of Science, ICT and Future Planning) (No. 2014M1A8A1049303), the Wearable Platform Materials Technology Center (WMC) funded by the National Research Foundation of Korea (NRF), a Grant of the Korean Government (MSIP) (No. 2016R1A5A1009926), and the BRL Program funded by the NRF (No. 2014R1A4A1003712). This work is also supported by the Global Ph.D. Fellowship Program through the National Research Foundation of Korea (NRF) funded by the Ministry of Education (No. 2015H1A2A1033952). The computational work done in Austin was supported by the Welch Foundation (F-1841) and the Texas Advanced Computing Center.

■ REFERENCES

(1) Debe, M. K. Electrocatalyst approaches and challenges for automotive fuel cells. *Nature* **2012**, *486* (7401), 43−51.

(2) Zeng, K.; Zhang, D. Recent progress in alkaline water electrolysis for hydrogen production and applications. *Prog. Energy Combust. Sci.* **2010**, *36*, 307−326.

(3) Man, I. C.; Su, H.-Y.; Calle-Vallejo, F.; Hansen, H. A.; Martínez, J. I.; Inoglu, N. G.; Kitchin, J.; Jaramillo, T. F.; Nørskov, J. K.; Rossmeisl, J. Universality in Oxygen Evolution Electrocatalysis on Oxide Surfaces. *ChemCatChem* **2011**, *3*, 1159−1165.

(4) McCrory, C. C.; Jung, S.; Peters, J. C.; Jaramillo, T. F. Benchmarking heterogeneous electrocatalysts for the oxygen evolution reaction. *J. Am. Chem. Soc.* **2013**, *135*, 16977−16987.

(5) Fabbri, E.; Habereder, A.; Waltar, K.; Kötz, R.; Schmidt, T. J. Developments and perspectives of oxide-based catalysts for the oxygen evolution reaction. *Catal. Sci. Technol.* **2014**, *4*, 3800−3821.

(6) Lee, Y.; Suntivich, J.; May, K. J.; Perry, E. E.; Shao-Horn, Y. Synthesis and Activities of Rutile IrO_2 and RuO_2 Nanoparticles for Oxygen Evolution in Acid and Alkaline Solutions. *J. Phys. Chem. Lett.* **2012**, *3*, 399−404.

(7) Lettenmeier, P.; Wang, L.; Golla-Schindler, U.; Gazdzicki, P.; Canas, N. A.; Handl, M.; Hiesgen, R.; Hosseiny, S. S.; Gago, A. S.; Friedrich, K. A. Nanosized IrO_x-Ir Catalyst with Relevant Activity for Anodes of Proton Exchange Membrane Electrolysis Produced by a Cost-Effective Procedure. *Angew. Chem., Int. Ed.* **2016**, *55*, 742−746.

DOI: 10.1021/acs.chemmater.8b02061
Chem. Mater. 2018, 30, 5941−5950

(8) AlYami, N. M.; LaGrow, A. P.; Joya, K. S.; Hwang, J.; Katsiev, K.; Anjum, D. H.; Losovyj, Y.; Sinatra, L.; Kim, J. Y.; Bakr, O. M. Tailoring ruthenium exposure to enhance the performance of fcc platinum@ruthenium core-shell electrocatalysts in the oxygen evolution reaction. *Phys. Chem. Chem. Phys.* **2016**, *18*, 16169−16178.
(9) Sun, W.; Song, Y.; Gong, X.-Q.; Cao, L.-m.; Yang, J. An efficiently tuned d-orbital occupation of IrO_2 by doping with Cu for enhancing the oxygen evolution reaction activity. *Chem. Sci.* **2015**, *6*, 4993−4999.
(10) Kwon, T.; Hwang, H.; Sa, Y. J.; Park, J.; Baik, H.; Joo, S. H.; Lee, K. Cobalt Assisted Synthesis of IrCu Hollow Octahedral Nanocages as Highly Active Electrocatalysts toward Oxygen Evolution Reaction. *Adv. Funct. Mater.* **2017**, *27*, 1604688.
(11) Wang, C.; Sui, Y.; Xiao, G.; Yang, X.; Wei, Y.; Zou, G.; Zou, B. Synthesis of Cu−Ir nanocages with enhanced electrocatalytic activity for the oxygen evolution reaction. *J. Mater. Chem. A* **2015**, *3*, 19669−19673.
(12) Nong, H. N.; Gan, L.; Willinger, E.; Teschner, D.; Strasser, P. IrO_x core-shell nanocatalysts for cost- and energy-efficient electrochemical water splitting. *Chem. Sci.* **2014**, *5*, 2955.
(13) Lim, J.; Yang, S.; Kim, C.; Roh, C. W.; Kwon, Y.; Kim, Y. T.; Lee, H. Shaped Ir-Ni bimetallic nanoparticles for minimizing Ir utilization in oxygen evolution reaction. *Chem. Commun.* **2016**, *52*, 5641−5644.
(14) Reier, T.; Pawolek, Z.; Cherevko, S.; Bruns, M.; Jones, T.; Teschner, D.; Selve, S.; Bergmann, A.; Nong, H. N.; Schlögl, R.; Mayrhofer, K. J. J.; Strasser, P. Molecular Insight in Structure and Activity of Highly Efficient, Low-Ir Ir−Ni Oxide Catalysts for Electrochemical Water Splitting (OER). *J. Am. Chem. Soc.* **2015**, *137*, 13031−13040.
(15) Nong, H. N.; Oh, H.-S.; Reier, T.; Willinger, E.; Willinger, M.-G.; Petkov, V.; Teschner, D.; Strasser, P. Oxide-Supported $IrNiO_x$ Core-Shell Particles as Efficient, Cost-Effective, and Stable Catalysts for Electrochemical Water Splitting. *Angew. Chem., Int. Ed.* **2015**, *54*, 2975−2979.
(16) Lee, B.-S.; Park, H.-Y.; Choi, I.; Cho, M. K.; Kim, H.-J.; Yoo, S. J.; Henkensmeier, D.; Kim, J. Y.; Nam, S. W.; Park, S.; Lee, K.-Y.; Jang, J. H. Polarization characteristics of a low catalyst loading PEM water electrolyzer operating at elevated temperature. *J. Power Sources* **2016**, *309*, 127−134.
(17) Lee, B.-S.; Ahn, S. H.; Park, H.-Y.; Choi, I.; Yoo, S. J.; Kim, H.-J.; Henkensmeier, D.; Kim, J. Y.; Park, S.; Nam, S. W.; Lee, K.-Y.; Jang, J. H. Development of electrodeposited IrO_2 electrodes as anodes in polymer electrolyte membrane water electrolysis. *Appl. Catal., B* **2015**, *179*, 285−291.
(18) Oh, H.-S.; Lim, K. H.; Roh, B.; Hwang, I.; Kim, H. Corrosion resistance and sintering effect of carbon supports in polymer electrolyte membrane fuel cells. *Electrochim. Acta* **2009**, *54*, 6515−6521.
(19) Oh, H. S.; Nong, H. N.; Reier, T.; Bergmann, A.; Gliech, M.; Ferreira de Araujo, J.; Willinger, E.; Schlogl, R.; Teschner, D.; Strasser, P. Electrochemical Catalyst-Support Effects and Their Stabilizing Role for IrO_x Nanoparticle Catalysts during the Oxygen Evolution Reaction. *J. Am. Chem. Soc.* **2016**, *138*, 12552−12563.
(20) Oakton, E.; Lebedev, D.; Povia, M.; Abbott, D. F.; Fabbri, E.; Fedorov, A.; Nachtegaal, M.; Copéret, C.; Schmidt, T. J. IrO_2-TiO_2: A High-Surface-Area, Active, and Stable Electrocatalyst for the Oxygen Evolution Reaction. *ACS Catal.* **2017**, *7*, 2346−2352.
(21) Mazúr, P.; Polonský, J.; Paidar, M.; Bouzek, K. Non-conductive TiO_2 as the anode catalyst support for PEM water electrolysis. *Int. J. Hydrogen Energy* **2012**, *37*, 12081−12088.
(22) Hu, W.; Chen, S.; Xia, Q. IrO_2/Nb−TiO_2 electrocatalyst for oxygen evolution reaction in acidic medium. *Int. J. Hydrogen Energy* **2014**, *39*, 6967−6976.
(23) Massue, C.; Pfeifer, V.; Huang, X.; Noack, J.; Tarasov, A.; Cap, S.; Schlogl, R. High-Performance Supported Iridium Oxohydroxide Water Oxidation Electrocatalysts. *ChemSusChem* **2017**, *10*, 1943−1957.
(24) Kwak, I.; Kwon, I. S.; Kim, J.; Park, K.; Ahn, J.-P.; Yoo, S. J.; Kim, J.-G.; Park, J. IrO2−ZnO Hybrid Nanoparticles as Highly Efficient Trifunctional Electrocatalysts. *J. Phys. Chem. C* **2017**, *121*, 14899−14906.
(25) Nikiforov, A. V.; Tomás García, A. L.; Petrushina, I. M.; Christensen, E.; Bjerrum, N. J. Preparation and study of IrO_2/SiC−Si supported anode catalyst for high temperature PEM steam electrolysers. *Int. J. Hydrogen Energy* **2011**, *36*, 5797−5805.
(26) Polonský, J.; Mazúr, P.; Paidar, M.; Christensen, E.; Bouzek, K. Performance of a PEM water electrolyser using a TaC-supported iridium oxide electrocatalyst. *Int. J. Hydrogen Energy* **2014**, *39*, 3072−3078.
(27) Polonský, J.; Petrushina, I. M.; Christensen, E.; Bouzek, K.; Prag, C. B.; Andersen, J. E. T.; Bjerrum, N. J. Tantalum carbide as a novel support material for anode electrocatalysts in polymer electrolyte membrane water electrolysers. *Int. J. Hydrogen Energy* **2012**, *37*, 2173−2181.
(28) Kim, H.; Cho, M. K.; Kwon, J. A.; Jeong, Y. H.; Lee, K. J.; Kim, N. Y.; Kim, M. J.; Yoo, S. J.; Jang, J. H.; Kim, H. J.; Nam, S. W.; Lim, D. H.; Cho, E.; Lee, K. Y.; Kim, J. Y. Highly efficient and durable TiN nanofiber electrocatalyst supports. *Nanoscale* **2015**, *7*, 18429−18434.
(29) Kim, N. Y.; Lee, J. H.; Kwon, J. A.; Yoo, S. J.; Jang, J. H.; Kim, H.-J.; Lim, D.-H.; Kim, J. Y. Vanadium nitride nanofiber membrane as a highly stable support for Pt-catalyzed oxygen reduction reaction. *J. Ind. Eng. Chem.* **2017**, *46*, 298−303.
(30) Kwon, J. A.; Kim, M.-S.; Shin, D. Y.; Kim, J. Y.; Lim, D.-H. First-principles understanding of durable titanium nitride (TiN) electrocatalyst supports. *J. Ind. Eng. Chem.* **2017**, *49*, 69−75.
(31) Chen, P.; Xu, K.; Fang, Z.; Tong, Y.; Wu, J.; Lu, X.; Peng, X.; Ding, H.; Wu, C.; Xie, Y. Metallic Co_4N Porous Nanowire Arrays Activated by Surface Oxidation as Electrocatalysts for the Oxygen Evolution Reaction. *Angew. Chem., Int. Ed.* **2015**, *54*, 14710−14714.
(32) Chen, P.; Xu, K.; Tong, Y.; Li, X.; Tao, S.; Fang, Z.; Chu, W.; Wu, X.; Wu, C. Cobalt nitrides as a class of metallic electrocatalysts for the oxygen evolution reaction. *Inorg. Chem. Front.* **2016**, *3*, 236−242.
(33) Yoon, K. R.; Kim, D. S.; Ryu, W. H.; Song, S. H.; Youn, D. Y.; Jung, J. W.; Jeon, S.; Park, Y. J.; Kim, I. D. Tailored Combination of Low Dimensional Catalysts for Efficient Oxygen Reduction and Evolution in Li-O_2 Batteries. *ChemSusChem* **2016**, *9*, 2080−2088.
(34) Yoon, K. R.; Ko, J. W.; Youn, D.-Y.; Park, C. B.; Kim, I.-D. Synthesis of Ni-based co-catalyst functionalized W:$BiVO_4$ nanofibers for solar water oxidation. *Green Chem.* **2016**, *18*, 944−950.
(35) Cho, S. H.; Jung, J. W.; Kim, C.; Kim, I. D. Rational Design of 1-D Co_3O_4 Nanofibers@Low content Graphene Composite Anode for High Performance Li-Ion Batteries. *Sci. Rep.* **2017**, *7*, 45105.
(36) Bonet, F.; Delmas, V.; Grugeon, S.; Herrera Urbina, R.; Silvert, P. Y.; Tekaia-Elhsissen, K. Synthesis of monodisperse Au, Pt, Pd, Ru and Ir nanoparticles in ethylene glycol. *Nanostruct. Mater.* **1999**, *11*, 1277−1284.
(37) Yoon, K. R.; Shin, K.; Park, J.; Cho, S. H.; Kim, C.; Jung, J. W.; Cheong, J. Y.; Byon, H. R.; Lee, H. M.; Kim, I. D. Brush-Like Cobalt Nitride Anchored Carbon Nanofiber Membrane: Current Collector-Catalyst Integrated Cathode for Long Cycle Li-O_2 Batteries. *ACS Nano* **2018**, *12*, 128−139.
(38) Kresse, G.; Furthmuller, J. Efficient iterative schemes for ab initio total-energy calculations using a plane-wave basis set. *Phys. Rev. B: Condens. Matter Mater. Phys.* **1996**, *54*, 11169−11186.
(39) Perdew, J. P.; Burke, K.; Ernzerhof, M. Generalized Gradient Approximation Made Simple. *Phys. Rev. Lett.* **1996**, *77*, 3865−3868.
(40) Blöchl, P. E. Projector augmented-wave method. *Phys. Rev. B: Condens. Matter Mater. Phys.* **1994**, *50*, 17953−17979.
(41) Jang, J. S.; Kim, S. J.; Choi, S. J.; Kim, N. H.; Hakim, M.; Rothschild, A.; Kim, I. D. Thin-walled SnO_2 nanotubes functionalized with Pt and Au catalysts via the protein templating route and their selective detection of acetone and hydrogen sulfide molecules. *Nanoscale* **2015**, *7*, 16417−16426.
(42) Zhong, X.; Liu, L.; Jiang, Y.; Wang, X.; Wang, L.; Zhuang, G.; Li, X.; Mei, D.; Wang, J.-g.; Su, D. S. Synergistic Effect of Nitrogen in

DOI: 10.1021/acs.chemmater.8b02061
Chem. Mater. 2018, 30, 5941−5950

Cobalt Nitride and Nitrogen-Doped Hollow Carbon Spheres for the Oxygen Reduction Reaction. *ChemCatChem* **2015**, *7*, 1826−1832.
(43) Chen, Z.; Higgins, D.; Yu, A.; Zhang, L.; Zhang, J. A review on non-precious metal electrocatalysts for PEM fuel cells. *Energy Environ. Sci.* **2011**, *4*, 3167−3192.
(44) Pfeifer, V.; Jones, T. E.; Velasco Velez, J. J.; Arrigo, R.; Piccinin, S.; Havecker, M.; Knop-Gericke, A.; Schlogl, R. In situ observation of reactive oxygen species forming on oxygen-evolving iridium surfaces. *Chem. Sci.* **2017**, *8*, 2143−2149.
(45) Pfeifer, V.; Jones, T. E.; Velasco Velez, J. J.; Massue, C.; Greiner, M. T.; Arrigo, R.; Teschner, D.; Girgsdies, F.; Scherzer, M.; Allan, J.; Hashagen, M.; Weinberg, G.; Piccinin, S.; Havecker, M.; Knop-Gericke, A.; Schlogl, R. The electronic structure of iridium oxide electrodes active in water splitting. *Phys. Chem. Chem. Phys.* **2016**, *18*, 2292−2296.
(46) Park, J.; Sa, Y. J.; Baik, H.; Kwon, T.; Joo, S. H.; Lee, K. Iridium-Based Multimetallic Nanoframe@Nanoframe Structure: An Efficient and Robust Electrocatalyst toward Oxygen Evolution Reaction. *ACS Nano* **2017**, *11*, 5500−5509.
(47) Li, T.; Kasian, O.; Cherevko, S.; Zhang, S.; Geiger, S.; Scheu, C.; Felfer, P.; Raabe, D.; Gault, B.; Mayrhofer, K. J. J. Atomic-scale insights into surface species of electrocatalysts in three dimensions. *Nat. Catal* **2018**, *1*, 300−305.
(48) Liang, F.; Yu, Y.; Zhou, W.; Xu, X.; Zhu, Z. Highly defective CeO_2 as a promoter for efficient and stable water oxidation. *J. Mater. Chem. A* **2015**, *3*, 634−640.
(49) Li, J.; Zhou, H.; Zhuo, H.; Wei, Z.; Zhuang, G.; Zhong, X.; Deng, S.; Li, X.; Wang, J. Oxygen vacancies on TiO_2 promoted the activity and stability of supported Pd nanoparticles for the oxygen reduction reaction. *J. Mater. Chem. A* **2018**, *6*, 2264−2272.

DOI: 10.1021/acs.chemmater.8b02061
Chem. Mater. 2018, 30, 5941−5950